# Generation of Annual Rossby Waves in the North Pacific

LAWRENCE A. MYSAK

*Departments of Mathematics and Oceanography, University of British Columbia, Vancouver, B.C., Canada V6T 1W5*

## ABSTRACT

A new mechanism is proposed for the generation of the annual-period baroclinic Rossby waves which have been observed in the central North Pacific by Kang and Magaard. It is shown that annual north–south fluctuations in the eastern boundary current off Vancouver Island can efficiently generate first baroclinic mode Rossby waves throughout the central North Pacific. In particular, to the southwest of Vancouver Island the direction, wavelength and speed of phase propagation associated with the far field (asymptotic) wave solution agree favorably with observations. Also, along any fixed latitude contained within the observed latitude band (30–40°N), the amplitudes of the vertical displacement at 300 m and surface horizontal current speed both monotonically increase to the west, in agreement with the observed trends for these quantities. However, the existence of this monotonicity in the solution appears to be quite sensitive to the north–south spatial structure of the fluctuating coastal current. For example, the oscillations of a point source (delta function) current excite a wave field with a fairly uniform amplitude across most of the observation region.

Within the context of a reduced gravity, quasi-geostrophic model, the theory presented here is quite general. For example, baroclinic waves of other than annual period could be investigated, and the radiation pattern due to a number of coastal sources could be determined.

## 1. Introduction

In a notable paper by Kang and Magaard (1980) (hereafter referred to as KM), convincing observational evidence was presented for annual-period baroclinic Rossby waves in the central North Pacific. In particular, Kang and Magaard showed that in the region 30–40°N, 130°W–160°E, these waves, as manifested in temperature records from depths of 250–400 m, have a first baroclinic mode vertical structure and travel northwestward with a typical wavelength of 300 km and a typical phase speed of 1 cm s$^{-1}$. Moreover, their group of velocity (direction of energy propagation) is approximately toward the southwest. To date, no comprehensive theory has been put forth which explains the observed propagation characteristics and generation mechanism of these waves. The purpose of this paper is to describe our attempt to provide such a theory.

From a consideration of Rossby wave kinematics together with the observations of KM (see Section 2), we infer that the source for the annual Rossby waves in the central North Pacific is most likely located just west of Vancouver Island. Recent current measurements made in this region by Howard Freeland (Institute of Ocean Sciences, Sidney, B.C.) indicate the presence of a large annual signal in the subsurface longshore flow. We hypothesize that these intense and localized *eastern boundary current fluctuations* provide the main vorticity source for the waves observed by KM. In so far as our wave source is located near the eastern coast, the theory presented here is similar to that of White and Saur (1981) and Krauss and Wuebber (1982) who investigated the generation of extratropical annual Rossby waves by annual variations in the winds along the eastern part of an ocean basin. However, in contrast to these studies, we assume here that the amplitude of the wave source has a relatively small north–south extent (a few hundred kilometers). White and Saur assumed that off California and Baja California (a north–south extent of 2000 km), the windstress curl has constant amplitude. Krauss and Wuebber modeled the north–south structure of the longshore winds off west Africa and Europe with a cos$\eta y$ function, where $\lambda = 2\pi \eta^{-1} \sim 6000$ km.

Our model differs significantly from those used by White and Saur (1981) and Krauss and Wuebber (1982) in other ways as well. White and Saur used a one-dimensional nondispersive long wave equation to model first baroclinic mode Rossby wave propagation, whereas we use the complete (dispersive) Rossby wave equation. The inclusion of all the dispersion terms is very essential if one is to obtain the northwestward direction of phase propagation observed by KM. Krauss and Wuebber used numerical methods to solve the dispersive wave equation, but with all the vertical modes taken into account. Nevertheless, they found that away from the coast, the response is dominated by the first baroclinic mode whose energy radiates nearly westward in the form of a long Rossby wave (wavelength $\sim 1800$ km). From these results it appears

that a reduced gravity model, which is used in this paper and which contains only the first baroclinic mode, faithfully represents the physical situation observed in the central North Pacific. Moreover, with such a model routine analytical methods can be used to find the solution.

Because the amplitude of the Rossby waves observed by KM in the latitude band 30–40°N increase monotonically west of 160°W, White and Saur (1981) suggeted that local windstress forcing may be the generating mechanism for these waves. Although the mid-ocean response to a variable windstress curl is larger than that due to either atmospheric pressure or buoyancy fluxes (Magaard, 1977), Krauss and Wuebber (1982) showed that the direct windstress generation of Rossby waves is not very efficient. Rather, a line source of windstress along the eastern coast is a much more significant forcing mechanism. Also, from the analysis of Gallegos–Garcia et al. (1981), there appears to be a large mismatch of atmospheric and oceanic wave scales at the annual period. They found that in the North Pacific region 16–40°N, 120–160°W the windstress curl spectrum was dominated by the annual period at long wavelengths (~2000–4000 km), which are about ten times the observed Rossby wavelengths (~300 km). Thus it is argued here that the waves observed by KM in the region 30–40°N, 130°W–160°E are not likely to be generated by the local winds. Remarkably enough, in the latitudinal band 30–40°N the coastal generation model presented here does predict a monotonic increase in wave amplitude west of 160°W, in agreement with the trend found by KM.

A discussion of the proposed coastal generation mechanism is given in Section 2, and the governing equations and boundary conditions are presented in Section 3. In Section 4 a Fourier integral solution of the relevant Rossby wave equation is obtained, and in Section 5 this solution is evaluated asymptotically by the method of steepest descent. The theoretical predictions are compared with the observations of KM in Section 6. The effects of refraction due to a variable Coriolis parameter are discussed qualitatively in Section 7. The conclusions are summarized in Section 8, where further theoretical and observational work are also suggested.

## 2. The generation mechanism

From an extensive set of XBT data covering the region 30–40°N, 130°W–160°E (TRANSPAC data), KM showed that in the subsurface layer 250–400 m the temperature fluctuations are composed of large-scale fluctuations (termed "quasi-homogeneous") with horizontal space scales comparable to the size of the North Pacific basin, and smaller scale fluctuations (termed "wavelike") with length scales of a few hundred kilometers. The quasi-homogeneous fluc-

tuations decrease monotonically with depth and are related to large-scale and long-term temperature anomalies at the sea surface (Kang, 1980). At the annual period, the wavelike fluctuations consist mainly of first baroclinic mode Rossby waves.

A cross-spectral wavenumber fit (see KM for details) was made to the wavelike part of the temperature fluctuations at the annual frequency. However, the best-fitting wavenumber vectors were determined without assuming any dispersion relation. The results are illustrated in Fig. 1, which shows the best-fitting wavenumber vectors in 35 subareas of the total area analyzed by KM. The consistent pattern of northwestward phase propagation is most evident. The typical wavelength is about 300 km and the corresponding (annual period) phase velocity is about 1 cm s$^{-1}$.

A comparison between the best-fitting wavenumbers and the slowness curve for free annual-frequency first baroclinic mode Rossby waves is given in Fig. 2 for subarea 4: 30–40°N, 150–170°W. For this subarea and subarea 3 immediately to the west (30–40°N, 170°W–170°E), the dispersion curves which take into account the observed mean stratification and mean shear have been computed by Kang and Magaard (1979). We note that the shear slowness curve (solid line) fits the data only marginally better than the shear free curve (dashed line). Indeed, because in the wavenumber region of interest (the cluster of seven dots) the two slowness curves are close together, it appears that the inclusion of shear in a Rossby wave model is not essential. Hence in the theoretical development contained in the subsequent section, we shall neglect the mean flow. This approximation was also made by White and Saur (1981).
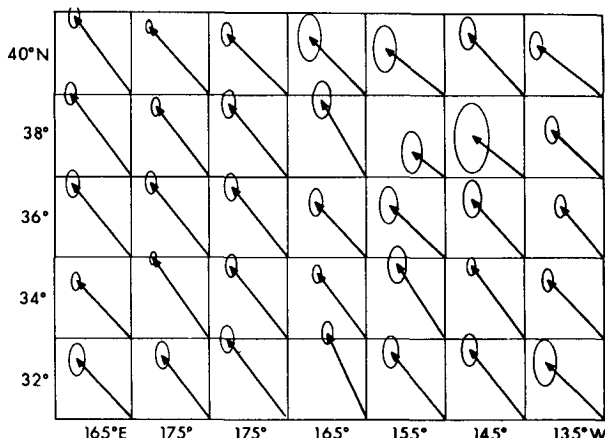


FIG. 1. The best-fit wavenumber vectors with error ellipses in the 35 subareas. Each square in this figure represents a wavenumber vector space of size 2 × 10$^{-5}$ m$^{-1}$ by 2 × 10$^{-5}$ m$^{-1}$, with the origin of the wavenumber coordinates at the lower right corner (Kang and Magaard, 1980).
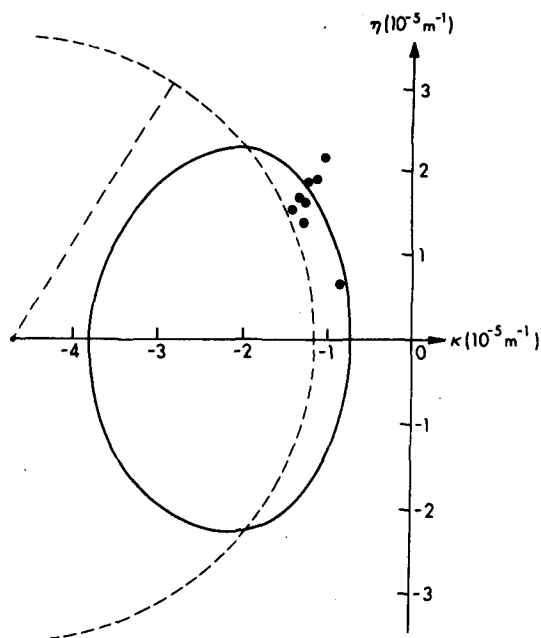
FIG. 2. The slowness curves $[\omega(\kappa, \eta) = $ constant, where $\omega(\kappa, \eta)$ is the dispersion relation for free Rossby waves] of the first baroclinic shear mode (solid line) and the ordinary shear free mode at the annual frequency for subarea 4 (30–40°N, 150–170°W). For the shear free mode the slowness curve is a circle (LeBlond and Mysak, 1978). The tips of the best-fit wavenumber vectors for the plane wave model of KM from the eight subareas contained in subarea 4 are shown by dots (Kang and Magaard, 1980).

Figure 3 shows the superposition of Fig. 2 on a map of the central North Pacific with subarea 4 at the center. The group velocity vector $c_g$ which is representative of the wavenumber data from subarea 4 is directed towards the center of the shear free slowness circle, in a southwestward direction. Since the energy of Rossby waves propagates along $c_g$, it is quite conceivable that

the source for the free (unforced) waves observed by KM is located in the northeast Pacific, just off Vancouver Island. Although in this region there is evidence (R. E. Thomson, personal communication, 1982) of a small annual signal in the alongshore wind with 5 m s$^{-1}$ amplitude, a more pronounced feature which could generate annual Rossby waves is the strong annual cycle in the subsurface eastern boundary current. This cycle has, for example, been recently observed by Howard Freeland (personal communication, 1982) at the continental slope station CZ4, located at 48°10.6′N, 125°56.2′W (see Fig. 3)[1]. Figure 4 shows the low pass currents observed during the two year period 1 June 1979–29 May 1981 at 4 depths (50, 100, 250, 500 m) at station CZ4. A fairly regular coastally aligned annual signal is seen in the top three current records, with northwestward flow during the fall and winter (September to February) and southwestward flow during the spring and summer (March to August). Recent measurements at 50 and 100 m from LPB, a station near CZ4 indicate that this annual variation persisted until spring 1981 (T. Yao, personal communication, 1982). A representative amplitude for the current fluctuations at 50 and 100 m is about 23 cm s$^{-1}$; for the 250 m fluctuations, a value of about 14 cm s$^{-1}$ is appropriate. Thus over the upper 300 m (the depth we use for the upper layer of our model in Section 3), an average value for the amplitude of the current fluctuations is 20 cm s$^{-1}$.

We emphasize that the annual signal illustrated in Fig. 4 appears to be quite localized in the north–south direction and to be confined to the continental slope or continental shelf regions. Inspection of data from

---

[1] We shall later see that this station is located just south of the cutoff latitude for the annual Rossby wave in our model.
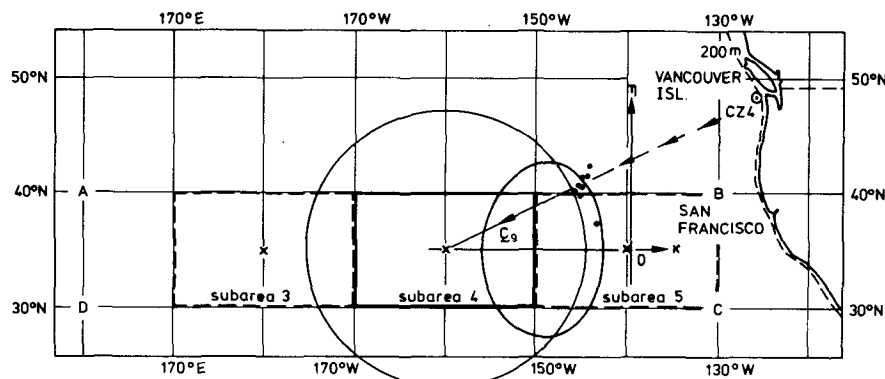


FIG. 3. Central North Pacific Ocean showing the area studied by KM (the rectangle ABCD) and the superposition of the subarea 4 data and slowness curves from Fig. 2. The group velocity vector of the annual waves observed by KM is shown to emanate from the Institute of Ocean Sciences' mooring Coastal Zone 4 (CZ4) located at 48°10.6′N, 125°56.2′W. Data from subarea 3 and 5 (dashed rectangles) will be presented later and also compared with theory (e.g., see Fig. 10).
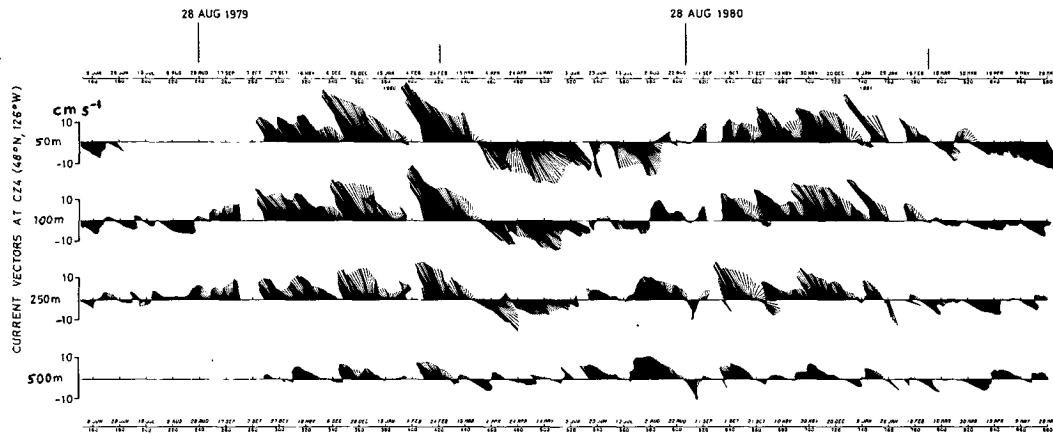
FIG. 4. Two year record of horizontal current velocity vectors at Institute of Ocean Sciences' mooring CZ4 (48°10.6'N, 125°56.2'W), where the water depth is 800 m. North is toward the top of the figure. (Data courtesy of Dr. Howard Freeland).

simultaneous slope and shelf moorings off Estevan point (about 150 km north of CZ4) revealed a less pronounced annual cycle there in the currents (R. E. Thomson, personal communication, 1982). Further south, off Oregon, there appears to be a regular annual signal in the alongshore current only on the shelf (Huyer et al., 1979). And off California, the longshore geostrophic flow of the California current at the surface and at 200 m (relative to 500 m) has a notable semi-annual cycle instead (D. Chelton, personal communication, 1982). The cause of the annual cycle near CZ4 is unknown. One hypothesis which deserves further study is that it may be due to the seasonal shift of the east–west axis of the west-wind drift in the North Pacific[2]. If during part of the fall and winter the axis is located at around 40–45°N, then when the flow hits the California–Oregon coast it must bifurcate, with northward flow occurring at CZ4 and southward flow occurring off southern California. On the other hand, if the axis is located at around 50–55°N during part of the spring and summer, then this will produce a southward flow off CZ4 and a northward flow along the Alaskan panhandle.

Let $x$, $y$ denote eastward and northward Cartesian coordinates on a midlatitude $\beta$-plane centered at latitude $\phi_0$. To model the region studied by KM, i.e. the latitude band 30–40°N, we shall later take $\phi_0 = 35°$. Since the annual current oscillations over the upper 250 m at CZ4 are coastally aligned and do not extend far offshore, we model them in this layer by an oscillating vortex sheet at $x = 0$:

$$v(0, y, t) = v_c(y - y_0)e^{-i\omega t}, \qquad (2.1)$$

where $v(0, y, t)$ is the northward velocity component

at the coast, $\omega > 0$ is the annual frequency and $v_c(y - y_0)$ is an amplitude function with argument $y - y_0$ which has a maximum at $y = y_0$ (i.e., at CZ4) and which falls off as $|y - y_0| \to \infty$. The two models for $v_c$ that we shall consider in this paper are

*model (a):*

$$v_c = Q\delta(y - y_0), \qquad (2.2)$$

*model (b):*

$$v_c = v_0 \exp(-|y - y_0|/L). \qquad (2.3)$$

Model (2.2) represents a point source velocity of total strength $Q$, and model (2.3) is a "tent-shaped" current with maximum speed $v_0$ at $y = y_0$ and an $e$-folding decay scale away from $y_0$ of $L$. From the observations of Freeland (Fig. 4) and R. E. Thomson, we choose $v_0 = 0.2$ m s$^{-1}$ and $L = 100$ km as representative values. Note that in the limit $L \to 0$ and $v_0 \to \infty$ such that $Lv_0 \to \frac{1}{2}Q$ model (2.3) reduces to (2.2). In the application of the theory to the North Pacific we shall find that the far field solutions are quite sensitive to the form of the amplitude function $v_c(y - y_0)$.

We note that the coastal current (2.1) effectively produces an infinitely large oscillating shear $(\partial v/\partial x)$ near the coast. Since Rossby waves are vorticity waves, this oscillating eastern boundary current behaves as a large vorticity source for the waves. An analogous concept was introduced recently by Mysak and Willmott (1981) who studied the generation of trench waves by oscillations in a western boundary current. It could be argued that the infinite shear in our model is unrealistic and that it would be better to use an oscillating boundary current with finite offshore extent and hence a finite lateral shear. Such a model, though worthwhile for study, is much more difficult to handle analytically, and its analysis is beyond the scope of this paper. In defence of our source model (2.1), we note that in tidal theory an oscillating current located at the boundary is commonly used

---

[2] Some evidence of such a seasonal shift can be seen in the paths taken by satellite tracked drogues west of British Columbia and Washington (Kirwan et al., 1978).

as a mechanism for the generation of long waves in the open ocean (e.g., see LeBlond and Mysak, 1978, Chapter 8).

## 3. Governing equations

Following other recent theoretical models of annual baroclinic Rossby waves in the North Pacific (e.g., White and Saur, 1981), we shall use the "1½-layer" or "reduced gravity" long wave equations for a mid-latitude $\beta$-plane:

$$u_t - fv + g'd_x = -r_0 u, \qquad (3.1a)$$

$$v_t + fu + g'd_y = -r_0 v, \qquad (3.1b)$$

$$H_0(u_x + v_y) + d_t = 0, \qquad (3.2)$$

where $x$, $y$ are the eastward and northward coordinates, $d$ the depth of the upper layer which overlies a deep motionless lower layer, $u$ and $v$ are the $x$ and $y$ components of velocity in the upper layer, $r_0 > 0$ is a Rayleigh damping friction coefficient, $f$ the Coriolis parameter (with $df/dy = \beta$, but otherwise treated as constant), $g'$ the reduced gravity ($=g\Delta\rho/\rho$ where $\rho$ is the lower layer density, $\rho - \Delta\rho$ is the upper layer density and $g$ is the gravitational acceleration) and $H_0$ is the mean depth of the upper layer, i.e.

$$d = H_0 + \zeta - h, \qquad (3.3)$$

where $\zeta$ is the free surface elevation and $h$ is the interfacial displacement. To a high degree of approximation,

$$d \approx H_0 - h \qquad (3.4)$$

for baroclinic motions.

We shall assume that $0 < r_0 \ll \omega$, where $\omega$ is a characteristic frequency. That is, the damping is assumed to be small. We shall eventually take the limit $r_0 \rightarrow 0$; however by retaining the damping terms on the right sides of (3.1a, b) in our analysis, we shall ensure that the radiation condition is satisfied.

Equations (3.1a, b) and (3.2) can be combined into a lengthy equation for $d$ [e.g., see Eq. (20.13a) in LeBlond and Mysak, 1978]. Under the assumptions that the $x$ and $y$ scales are comparable and that $|(\partial_t + r_0)d| \ll |fd|$, this equation reduces to the standard Rossby wave equation

$$(\partial_t + r_0)(\nabla^2 - 1/R^2)d + \beta d_x = 0, \qquad (3.5)$$

where $\nabla^2 = \partial_{xx} + \partial_{yy}$ and $R = (g'H_0)^{1/2}/f$ is the internal Rossby radius. We shall assume (3.5) holds in the semi-infinite domain $x < 0$, $|y| < \infty$. At $x = 0$ we require $u = 0$, which, when substituted into (3.1a), gives[3]

---

[3] Note that (3.6) implies the existence of annual fluctuations in the isopycnal slope near the coast. Such fluctuations have recently been observed over the continental slope region near CZ4, but not further offshore along line P which extends to the WNW from CZ4 (S. Tabata, personal communication). These observations thus strengthen our hypothesis that the generation source is coastally confined.

$$d_x = (f/g')v(0, y, t) \quad \text{at} \quad x = 0, \qquad (3.6)$$

where $v(0, y, t) = v_c(y - y_0)e^{-i\omega t}$ is the prescribed velocity along the coast [see (2.1)]. For large $x$ and $y$ we require the solution to be bounded.

In view of the periodic form of $v(0, y, t)$, we let $d = D(x, y)e^{-i\omega t}$. Then (3.5) and the boundary conditions reduce to

$$(-i\omega + r_0)(\nabla^2 - 1/R^2)D + \beta D_x = 0,$$

$$x < 0 \quad \text{and} \quad |y| < \infty, \qquad (3.7)$$

$$D_x = (f/g')v_c(y - y_0) \quad \text{at} \quad x = 0, \qquad (3.8)$$

$$|D| < \infty \quad \text{as} \quad (x^2 + y^2)^{1/2} \rightarrow \infty. \qquad (3.9)$$

For free plane wave solutions $D \propto e^{i(\kappa x + \eta y)}$, (3.7) with $r_0 = 0$ yields the dispersion relation

$$\omega = \frac{-\beta\kappa}{k^2 + 1/R^2}, \qquad (3.10)$$

where $k^2 = \kappa^2 + \eta^2$. For the cluster of seven points shown in Fig. 2, an average value of $k$ is $2.12 \times 10^{-5}$ m$^{-1}$ (this was obtained from the data given in Table 1 of KM). Thus $k^2 = 4.49 \times 10^{-10}$ m$^{-2}$. For $H_0 = 300$ m, $g = 10$ m s$^{-2}$, $\Delta\rho/\rho = 3 \times 10^{-3}$ [values used by White and Saur (1981)], and $f = 0.837 \times 10^{-4}$ s$^{-1}$ (corresponding to a latitude of $\phi_0 = 35°$), we find $R = 35.83$ km and hence $1/R^2 = 7.79 \times 10^{-10}$ m$^{-2}$. Thus $k^2 \sim 1/R^2$ for the Rossby waves observed by KM, and it is not permissible to use the long wave dispersion relation $\omega = -\beta\kappa R^2$, or equivalently, the one-dimensional wave equation obtained from (3.7) by neglecting the operator $\nabla^2$.

From (3.10) we obtain the slowness curve

$$(\kappa + \gamma)^2 + \eta^2 = \gamma^2 - 1/R^2 \equiv K_1^2, \qquad (3.11)$$

where $\gamma = \beta/2\omega > 0$, which is a circle of radius $K_1$ centered at $(\kappa, \eta) = (-\gamma, 0)$. The critical or cut-off latitude beyond which a wave of fixed frequency cannot propagate is given by $K_1 = 0$, or

$$\tan\phi_0 = (g'H_0)^{1/2}/2R_e\omega, \qquad (3.12)$$

where $R_e$ is the radius of the Earth. For the annual frequency, we have $\omega = 1.99 \times 10^{-7}$ s$^{-1}$, and Eq. (3.12) thus yields

$$\tan\phi_0 = 1.128$$

for $R_e = 6.4 \times 10^6$ m and the $g'$, $H_0$ values given above. Thus $\phi_0 = 49.67°$ for our model, which is about one and a half degrees north of CZ4, our proposed source for the waves observed by KM. Hence we conclude that it is physically possible for annual Rossby wave energy to propagate from CZ4 to the more southerly observational region of KM.

Far from the source region of the waves, we expect our solution to have a free wave character. Accordingly, the slowness circle (3.11) should be a close approxi-

mation to KM's slowness circle shown in Fig. 2. At a latitude of 35° and at the annual frequency, $\gamma = 4.70 \times 10^{-5}$ m$^{-1}$ and thus the radius of our cirlce (3.11) is $K_1 = 3.78 \times 10^{-5}$ m$^{-1}$. Fig. 5 shows that our circle is just slightly larger than KM's and is also a good fit to the observed data.

## 4. Integral representation of solution

We define the Fourier transform $\tilde{D}(x, l)$ of $D(x, y)$ by

$$\tilde{D}(x, l) = \int_{-\infty}^{\infty} e^{ily}D(x, y)dy \equiv \mathcal{F}\{D\}. \quad (4.1)$$

Applying (4.1) to (3.7) yields

$$(-i\omega + r_0)[\tilde{D}_{xx} - (l^2 + 1/R^2)\tilde{D}] + \beta\tilde{D}_x = 0,$$

$$x < 0. \quad (4.2)$$

For $0 < \epsilon = r_0/\omega \ll 1$, the solution of (4.2) which satisfies (3.9) is given by

$$\tilde{D}(x, l) = A(l)e^{-i\gamma x - \epsilon\gamma x} \exp[x(l^2 - l_\epsilon^2)^{1/2}], \quad (4.3)$$

where $l_\epsilon = K_1(1 - i\epsilon\gamma^2/K_1^2)$ and $A(l)$ is a constant of integration to be determined from (3.8). The branches of $(l^2 - l_\epsilon^2)^{1/2}$ are chosen so that arg$(l^2 - l_\epsilon^2)^{1/2} \to 0$ as $l \to \pm\infty$. Thus from the branch point $l = l_\epsilon$ located in the fourth quadrant, we extend the branch cut downward, and from the branch point $l = -l_\epsilon$ in the second quadrant, we extend the branch cut upward. When $\epsilon \neq 0$, the Fourier inversion path is along the Re($l$) axis. In the limit $\epsilon \to 0(r_0 \to 0)$, corresponding to no friction, $l_\epsilon \to K_1$ and the branch points are located at $l = \pm K_1$. The inversion path $\Gamma$ is then indented around these points in the manner shown in Fig. 6.

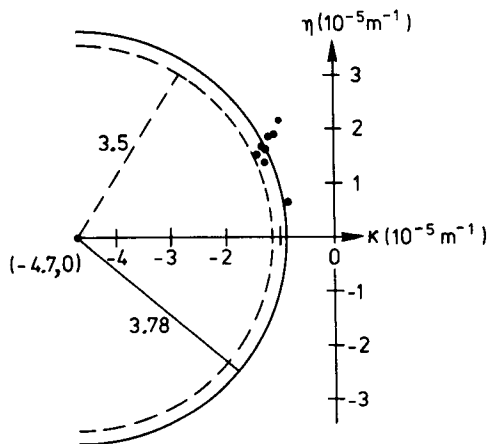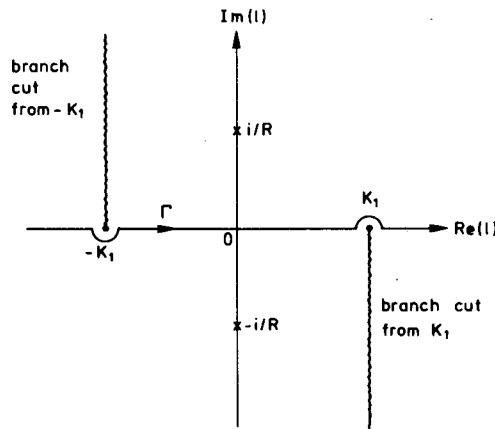Substituting (4.3) with $\epsilon = 0$ into the Fourier transform of (3.8) yields

FIG. 6. The inversion path $\Gamma$ in the $l$-plane when $r_0 = 0$ (no friction). The points $l = \pm i/R$ are simple poles of $A(l)$.

$$A(l) = \frac{(f/g')\tilde{v}_c(l)}{-i\gamma + (l^2 - K_1^2)^{1/2}}$$

$$= \frac{(f/g')\tilde{v}_c(l)[i\gamma + (l^2 - K_1^2)^{1/2}]}{l^2 + 1/R^2}, \quad (4.4)$$

where $\tilde{v}_c(l) = \mathcal{F}\{v_c(y - y_0)\}$. Hence for $\epsilon = 0$, $d = De^{-i\omega t}$ is given by

$$d(x, y, t) = \frac{e^{-i(\gamma x + \omega t)}}{2\pi} \int_\Gamma A(l)$$

$$\times \exp[x(l^2 - K_1^2)^{1/2} - ily]dl, \quad (4.5)$$

where $A(l)$ is given by (4.4) and $\Gamma$ is illustrated in Fig. 6, a contour which is consistent with that used by Mysak and LeBlond (1972). Note that the integrand in (4.5) has the following singularities: branch points at $l = \pm K_1$, simple poles at $l = \pm i/R$ and simple poles at $l = \pm i/L$ if $v_c$ is given by (2.3), since in this case,

model (b):

$$\tilde{v}_c = \frac{(2v_0/L)e^{ily_0}}{l^2 + 1/L^2}. \quad (4.6)$$

For the point source velocity (2.2),

model (a):

$$\tilde{v}_c = Qe^{ily_0}. \quad (4.7)$$

which is regular for all $l$.

Using the second form for $A(l)$ given in (4.4), we can write $d$ as the sum of two related integrals. Letting $F(x, t) = (f/g')e^{-i\gamma x - i\omega t}$, we find

$$d/F = i\gamma I_1 + (\partial/\partial x)I_1, \quad (4.8)$$

where

$$I_1 = \frac{1}{2\pi} \int_\Gamma \frac{\tilde{v}_c(l)}{l^2 + 1/R^2}$$

$$\times \exp[x(l^2 - K_1^2)^{1/2} - ily]dl. \quad (4.9)$$

Let

$$\tilde{f}_1(l) = \frac{\tilde{v}_c(l)}{l^2 + 1/R^2} \equiv \mathcal{F}\{f_1(y)\}, \quad (4.10)$$

$$\tilde{f}_2(x, l) = \exp[x(l^2 - K_1{}^2)^{1/2}] \equiv \mathcal{F}\{f_2(x, y)\}. \quad (4.11)$$

Then by the convolution theorem for Fourier transforms,

$$I_1 = \int_{-\infty}^{\infty} f_1(y - y')f_2(x, y')dy'. \quad (4.12)$$

Using the inverse Fourier transform relation

$$f_1(y) = \frac{1}{2\pi} \int_{-\infty}^{\infty} \tilde{f}_1(l)e^{-ily}dl, \quad (4.13)$$

$f_1$ can be readily found for $\tilde{v}_c(l)$ given by (4.6) or (4.7). Inspection of the transform pair Number 867 in Campbell and Foster (1948) together with (4.11) reveals that

$$f_2(x, y) = \frac{ixK_1 H_1^{(2)}[K_1(x^2 + y^2)^{1/2}]}{2(x^2 + y^2)^{1/2}}; \quad (4.14)$$

thus from (4.8), (4.12) and (4.14) it follows that

$$d = \frac{iK_1 f e^{-i(\gamma x + \omega t)}}{2g'} \int_{-\infty}^{\infty} \frac{f_1(y - y')}{(x^2 + y'^2)^{1/2}}$$

$$\times \left\{(1 + i\gamma x)H_1^{(2)}[K_1(x^2 + y'^2)^{1/2}]\right.$$

$$\left. - \frac{x^2 K_1}{(x^2 + y'^2)^{1/2}} H_2^{(2)}(K_1(x^2 + y'^2)^{1/2})\right\}dy'. \quad (4.15)$$

Hence for any coastal velocity profile $v_c$ for which $f_1$ can be found by inverting (4.10), we can compute $d$ from (4.15) by numerical integration. Since the Hankel function $H_1^{(2)}$ and $H_2^{(2)}$ are oscillatory, it follows from (4.15) that $d$ has an oscillatory spatial profile which propagates westward and which generally decreases in amplitude as $x \rightarrow -\infty$. Thus to get the actual thickness of the upper layer we must add $H_0$ to the solution (4.15). This of course is permissible since the solution of the original problem (3.5), (3.6) with $r_0 = 0$ is unique up to an additive constant. The solution (4.15) [or equivalently (4.5)] therefore represents the negative of the interfacial displacement $h$ [see (3.4)].

Instead of evaluating (4.15) numerically for all $x$ and $y$, we shall find in Section 5 the far-field solution from the integral representation (4.5), which we rewrite here in the form

$$d = \frac{f e^{-i(\gamma x + \omega t)}}{2\pi g'} \int_{\Gamma} \frac{\tilde{v}_c(l)}{-i\gamma + (l^2 - K_1{}^2)^{1/2}}$$

$$\times \exp[x(l^2 - K_1{}^2)^{1/2} - ily]dl. \quad (4.16)$$

Invoking the geostrophic relations, $u = -(g'/f)d_y$, $v = (g'/f)d_x$, Eq. (4.16) yields

$$u = \frac{e^{-i(\gamma x + \omega t)}}{2\pi} \int_{\Gamma} \frac{il\tilde{v}_c(l)}{-i\gamma + (l^2 - K_1{}^2)^{1/2}}$$

$$\times \exp[x(l^2 - K_1{}^2)^{1/2} - ily]dl, \quad (4.17)$$

$$v = \frac{e^{-i(\gamma x + \omega t)}}{2\pi} \int_{\Gamma} \tilde{v}_c(l) \exp[x(l^2 - K_1{}^2)^{1/2} - ily]dl. \quad (4.18)$$

Before evaluating the integrals in (4.16)–(4.18) asymptotically, it is instructive to note that for the point source velocity model (a) an explicit form for $v$ can be found. In this case $\tilde{v}_c = Qe^{ily_0}$ [see (4.7)], and Eq. (4.18) yields

$$v = \frac{ixK_1 Q e^{-i(\gamma x + \omega t)} H_1^{(2)}\{K_1[x^2 + (y - y_0)^2]^{1/2}\}}{2[x^2 + (y - y_0)^2]^{1/2}} \quad (4.19)$$

upon using Number 867 in Campbell and Foster (1948). Introducing polar coordinates centered at $x = 0$, $y = y_0$, viz.,

$$x = r\cos\theta, \quad y - y_0 = r\sin\theta, \quad (4.20)$$

where $\pi/2 < \theta < 3\pi/2$, Eq. (4.19) gives

$$v = \frac{1}{2}K_1 Q|\cos\theta|e^{-i(\gamma x + \omega t + \pi/2)}H_1^{(2)}(K_1 r). \quad (4.21)$$

Using the asymptotic form of $H_1^{(2)}$ for large argument [Abramowitz and Stegun, 1965, Eq. (9.2.4)] in (4.21), we arrive at the far-field solution

$$v \sim \frac{K_1 Q|\cos\theta|}{(2\pi K_1 r)^{1/2}} e^{-i(\gamma x + \omega t + K_1 r - \pi/4)}$$

$$\text{as} \quad K_1 r \rightarrow \infty. \quad (4.22)$$

For $y < y_0$ (i.e., to the south and west of the wave source), (4.22) represents a travelling wave with a westward component and a radial component directed toward the source (i.e., to the northeast). The resultant of these two components at any fixed point is a wave whose phase travels to the northwest, which is in qualitative agreement with the observations of KM. Similarly, for $y = y_0$ or $y > y_0$, (4.22) represents respectively a westward or southwestward travelling wave. In the next section we shall show that the far-field solutions for $d$ and $u$ also have these propagation characteristics. Further, for more general forms of $v_c(y - y_0)$ which decay as $|y - y_0| \rightarrow \infty$, we shall find that only the amplitude of the waves is altered; the direction of propagation remains unchanged.

## 5. Asymptotic solution

We now determine the far-field behavior of $d$, $u$ and $v$ by applying the method of steepest descent to the integrals (4.16)–(4.18). Since we have assumed $v_c = v_c(y - y_0)$, it follows that $\tilde{v}_c(l)$ has the form

$$\tilde{v}_c(l) = V_c(l)e^{ily_0}. \quad (5.1)$$

For velocity models (a) and (b),

$$V_c(l) = Q, \quad (5.2)$$

and

$$V_c(l) = \frac{2v_0/L}{l^2 + 1/L^2}, \qquad (5.3)$$

respectively [see (4.6) and (4.7)]. The presence of the factor $e^{il y_0}$ in (5.1) motivates introducing the source-centered polar coordinates $(r, \theta)$ defined in (4.20). Thus letting $l = K_1\lambda$, we find (4.16)–(4.18) take the form

$$d = \frac{fe^{-i(\gamma x + \omega t)}}{2\pi g'} \int_C \frac{V_c(K_1\lambda)e^{K_1 r f(\lambda)}}{-i\gamma/K_1 + (\lambda^2 - 1)^{1/2}} d\lambda, \quad (5.4)$$

$$u = \frac{iK_1 e^{-i(\gamma x + \omega t)}}{2\pi} \int_C \frac{\lambda V_c(K_1\lambda)e^{K_1 r f(\lambda)}}{-i\gamma/K_1 + (\lambda^2 - 1)^{1/2}} d\lambda, \quad (5.5)$$

$$v = \frac{e^{-i(\gamma x + \omega t)}}{2\pi} \int_C V_c(K_1\lambda)e^{K_1 r f(\lambda)} d\lambda, \qquad (5.6)$$

where

$$f(\lambda) = -|\cos\theta|(\lambda^2 - 1)^{1/2} - i\lambda \sin\theta \qquad (5.7)$$

and $C$ is analogous to $\Gamma$, but with indentations below $\lambda = -1$ and above $\lambda = 1$. For velocity model (a) the integrands of $d$ and $u$ have simple poles at $\lambda = \pm i/RK_1$; for velocity model (b), the integrands of $d$, $u$ and $v$ also have poles at $\lambda = \pm i/LK_1$.

The integrals in (5.4)–(5.6) are now in a convenient form to evaluate asymptotically for $K_1 r \gg 1$ by the method of steepest descent. Since $K_1 \sim 4 \times 10^{-5}$ m$^{-1}$ for the annual Rossby wave (see Fig. 5), the asymptotic expansions will be valid for $r \gg 25$ km, i.e. a few hundred or more kilometers from the source region. The saddle point $\lambda_s$ is that point for which $f'(\lambda_s) = 0$. Thus $\lambda_s = \sin\theta$, and hence (5.7) gives $f(\lambda_s) = -i$ and $f''(\lambda_s) = i/\cos^2\theta$. The path of steepest descent $C_s$ is the locus on which Im$[f(\lambda) - f(\lambda_s)] = 0$. Letting $\lambda = \lambda_1 + i\lambda_2$ it follows that $C_s$ is given by

$$\lambda_2 = \frac{(\lambda_1 - \sin\theta)(1 - \lambda_1 \sin\theta)}{|\cos\theta|(\lambda_1^2 - 2\lambda_1 \sin\theta + 1)^{1/2}}, \qquad (5.8)$$

which is illustrated in Fig. 7 for various ranges of $\sin\theta$. For $|\tan\theta| < 1/RK_1$ the inversion path C can be deformed into $C_s$ without crossing the poles at $\lambda = \pm i/RK_1$, and the asymptotic representation of $d$ say, is given by the saddle point contribution alone, provided of course $V_c(K_1\lambda)$ is regular. Since the latter is true only for the point source velocity it is important to distinguish between velocity profiles (a) and (b), for which

*model (a):*

$$V_c(K_1\lambda) = Q, \qquad (5.9)$$

*model (b):*

$$V_c(K_1\lambda) = \frac{2v_0/L}{K_1^2\lambda^2 + 1/L^2}. \qquad (5.10)$$

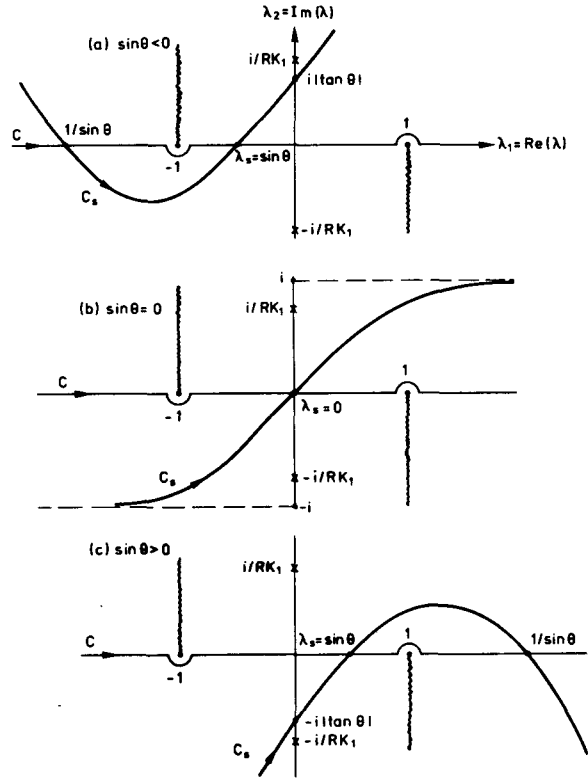For model (a) the asymptotic representation of (5.4) is given by



FIG. 7. The path of steepest descent $C_s$, as given by (5.8), for different ranges of $\sin\theta$.

$$d \sim \frac{fQK_1|\cos\theta| \exp[-i(\gamma x + K_1 r + \omega t - 3\pi/4)]}{g'(\gamma - K_1|\cos\theta|)(2\pi K_1 r)^{1/2}}$$

$$\equiv d_{sa}, \quad \text{for} \quad |\tan\theta| < 1/RK_1, \qquad (5.11)$$

$$d \sim d_{sa} + (fQ\gamma R/g') \exp[-|y - y_0|/R - i(\omega t - \pi/2)]$$

$$\equiv d_{sa} + d_{Ra}, \quad \text{for} \quad |\tan\theta| > 1/RK_1, \qquad (5.12)$$

where the second term in (5.12) represents the contribution from the pole at $i/RK_1$ when $\sin\theta < 0$ and $-\sin\theta/|\cos\theta| > 1/RK_1$ or from the pole at $(-i/RK_1)$ when $\sin\theta > 0$ and $\sin\theta|\cos\theta| > 1/RK_1$. In (5.11) and (5.12) the branch of $\tan\theta$ used is that for which $\pi/2 < \theta < 3\pi/2$. Similarly, the asymptotic representation of (5.5) and (5.6) for model (a) are given by

$$u \sim \frac{K_1^2 Q \sin\theta|\cos\theta| \exp[-i(\gamma x + K_1 r + \omega t - 5\pi/4)]}{(\gamma - K_1|\cos\theta|)(2\pi K_1 r)^{1/2}}$$

$$\equiv u_{sa}, \quad \text{for} \quad |\tan\theta| < 1/RK_1, \qquad (5.13)$$

$$u \sim u_{sa} + \text{sgn}(y - y_0)\gamma Q$$

$$\times \exp[-|y - y_0|/R - i(\omega t - \pi/2)] \equiv u_{sa} + u_{Ra},$$

$$\text{for} \quad |\tan\theta| > 1/RK_1, \qquad (5.14)$$

$$v \sim \frac{K_1 Q|\cos\theta| \exp[-i(\gamma x + K_1 r + \omega t - \pi/4)]}{(2\pi K_1 r)^{1/2}}$$

$$\equiv v_{sa}, \quad \text{for} \quad \pi/2 < \theta < 3\pi/2. \qquad (5.15)$$

Note that (5.15) agrees with (4.22), which was obtained after first integrating (4.18) (or equivalently (5.6)) explicitly.

Inside the sector $|\tan\theta| < 1/RK_1$ (see Fig. 8), only the saddle point contributions arise in the solutions for $d$, $u$ and $v$. On the line $\theta = \pi(y = y_0)$, $u_{sa} = 0$ whereas $d_{sa}$ and $v_{sa}$ fall off monotonically like $r^{-1/2}$. Also, along this line the wave form in (5.11) and (5.15) is locally plane and travels westward with speed $\omega/(\gamma - K_1)$ (see Fig. 9a). For other values of $\theta$ the saddle point contributions consist of a cylindrical wave travelling radially inward toward $x = 0$, $y = y_0$ together with a westward travelling component. The resultant is a wave whose phase travels to the southwest if $y > y_0(\theta < \pi)$, and to the northwest if $y < y_0(\theta > \pi)$. Since the wavenumbers in the exponent are independent of the excitation parameters the resultant wavenumber vector always lies on the slowness circle for free Rossby waves (see Fig. 9). Hence the wave energy propagates toward the center of this circle. From these arguments it follows that westward travelling waves have the longest wavelength $[=2\pi/(\gamma - K_1)]$. This result qualitatively explains why the annual waves travelling westward from southern California toward Hawaii (White and Saur, 1981) tend to be longer than those travelling northwestward in the region north of Hawaii (KM) (see Fig. 9a, c).

Outside the sector $|\tan\theta| < 1/RK_1$ (i.e., the shaded region in Fig. 8), the pole contributions in $d$ and $u$ consist of non-propagating disturbances which die out exponentially as $|y - y_0| \rightarrow \infty$. Since their e-folding scale is the Rossby radius $R$ ($\sim$35 km) and



FIG. 9. The resultant wavenumber vectors $\mathbf{k}_{res}$ for different values of latitude $y$. $y = y_0$ is the latitude of the wave source S (see Fig. 8).
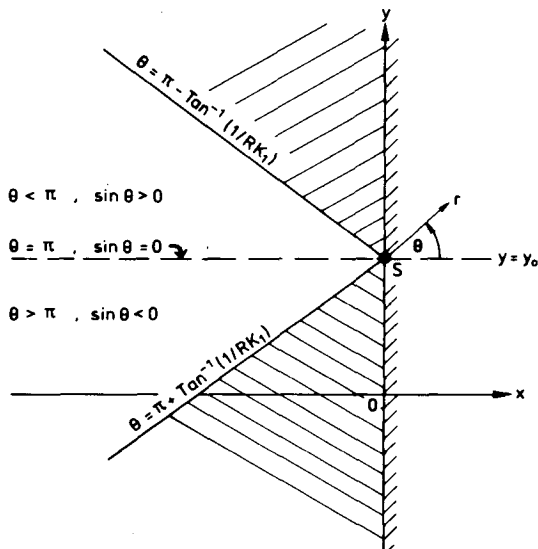


FIG. 8. The Stokes lines $\theta = \pi \pm \tan^{-1}(1/RK_1)$ (where $\tan^{-1}$ denotes principle branch) which emanate from the wave source S. Inside the undashed sector only the saddle point contributions arise in the far-field solutions. In the cross-hatched regions there are additional exponentially decaying contributions due to the poles.
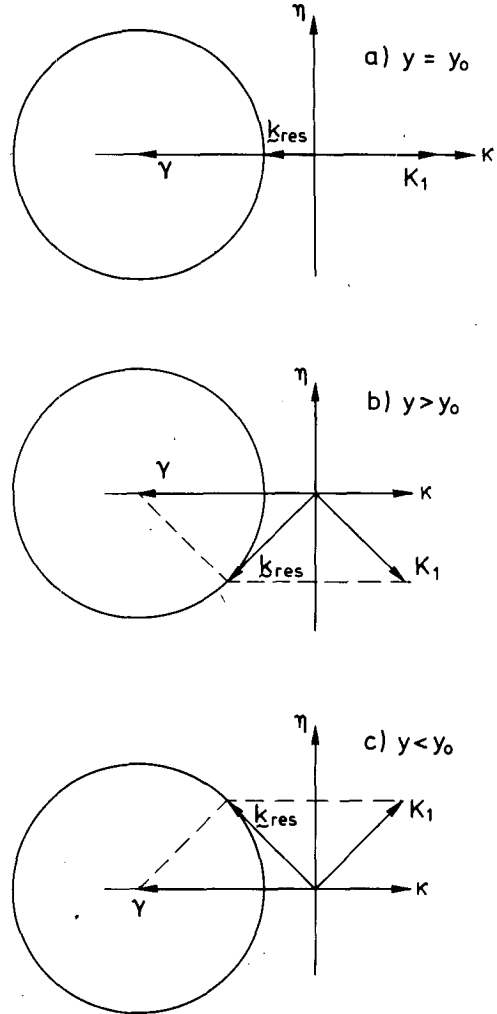
our solutions are valid for $r \gg 25$ km, these contributions are negligible.

For model (b) the $\theta$-dependence of the saddle point contributions is now different because $V_c(K_1\lambda)$ depends on $\lambda$ [see (5.10)]. Also, because of the additional poles at $\lambda = \pm i/LK_1$, there will be further contribution for $d$, $u$ and $v$ when $|\tan\theta| > 1/LK_1$. Hence under the realistic assumption that $L > R$, we find that

$$d \sim d_{sa} \frac{2v_0 L/Q}{1 + (LK_1 \sin\theta)^2} \equiv d_{sb},$$

$$\text{for} \quad |\tan\theta| < 1/LK_1, \tag{5.16}$$

$$d \sim d_{sb} + \frac{fv_0}{g'K_1} \exp[-|y - y_0|/L - i(k_1x + \omega t - \pi/2)]$$

$$\equiv d_{sb} + d_{Lb}, \quad \text{for} \quad 1/LK_1 < |\tan\theta| < 1/RK_1, \tag{5.17}$$

$$d \sim d_{sb} + d_{Lb} + d_{Ra} \frac{(2v_0L/Q)R^2}{R^2 - L^2},$$

$$\text{for } |\tan\theta| > 1/RK_1, \tag{5.18}$$

where $k_1 = \gamma - (K_1^2 + 1/L^2)^{1/2}$ and $d_{sa}, d_{Ra}$ are defined in (5.11), (5.12) respectively. If we set $Q = 2v_0L$, then inspection of (5.16) reveals that a spatially distributed coastal velocity such as model (b) tends to decrease the amplitude of the saddle point contribution since the factor $[1 + (LK_1 \sin\theta)^2]^{-1} \leqslant 1$ for $\pi/2 < \theta < 3\pi/2$. Also, such a profile produces a westward propagating (if $k_1 > 0$) plane wave $d_{Lb}$ in the region above and below the Stokes lines $\theta = \pi \pm \tan^{-1}(1/LK_1)$. However, as this decays exponentially as $|y - y_0| \rightarrow \infty$ with an $e$-folding scale of $L$, this contribution will be small in the far-field unless $L$ is unrealistically large ($\geqslant 1000$ km). Finally, we note that the non-propagating pole contribution in (5.18) is smaller than that in the point source solution by a factor of order $R^2/L^2 \ll 1$ and hence is again negligible. Thus we conclude that in the far-field region $r \geqslant 1000$ km, $\pi/2 < \theta < 3\pi/2$, the asymptotic solution for $d$ will be dominated by the saddle point contribution $d_{sb}$. The same also applies for $u$ and $v$, though, for completeness we give below both the saddle point and pole contributions for $K_1r \gg 1$:

$$u \sim u_{sa} \frac{2v_0L/Q}{1 + (LK_1 \sin\theta)^2} \equiv u_{sb},$$

$$\text{for } |\tan\theta| < 1/LK_1, \tag{5.19}$$

$$u \sim u_{sb} + \frac{v_0 \, \mathrm{sgn}(y - y_0)}{Lk_1} \exp[-|y - y_0|/L$$

$$- i(k_1x + \omega t - \pi/2)] \equiv u_{sb} + u_{Lb},$$

$$\text{for } 1/LK_1 < |\tan\theta| < 1/RK_1, \tag{5.20}$$

$$u \sim u_{sb} + u_{Lb} + u_{Ra} \frac{(2v_0L/Q)R^2}{R^2 - L^2},$$

$$\text{for } |\tan\theta| > 1/RK_1, \tag{5.21}$$

and

$$v \sim v_{sa} \frac{2v_0L/Q}{1 + (LK_1 \sin\theta)^2} \equiv v_{sb},$$

$$\text{for } |\tan\theta| < 1/LK_1, \tag{5.22}$$

$$v \sim v_{sb} + v_0 \exp[-|y - y_0|/L - i(k_1x + \omega t)],$$

$$\text{for } |\tan\theta| > 1/LK_1, \tag{5.23}$$

where $u_{sa}, u_{Ra}$ and $v_{sa}$ are defined in (5.13), (5.14) and (5.15) respectively.

## 6. Comparison of theory with observations of KM

There are two separate aspects of the KM observations that we now compare with the theory developed in this paper: 1) the propagation properties of

the waves (Figs. 1 and 2); and 2) the amplitude distribution of the wave fields (see Figs. 11 and 12). In making the comparison of the theory with these two aspects, only the saddle point contributions of the asymptotic solutions were used. This is because the distance from the source $S$ to the nearest corner of the observation region of KM (point B in Fig. 3) is over 1000 km; for $r \geqslant 1000$ km the pole contributions are insignificant for all $\pi/2 < \theta < 3\pi/2$.

In the expression for the saddle point contributions $d_{sa}, d_{sb}, u_{sa}, \ldots$, the following parameter values have been used in the computations:

$$\left.\begin{aligned}
g &= 10 \text{ m s}^{-2} \\
H_0 &= 300 \text{ m} \\
\Delta\rho/\rho &= 3 \times 10^{-3} \\
f &= 0.837 \times 10^{-4} \text{ s}^{-1} \text{ (latitude } \phi_0 = 35°) \\
R &= (gH_0\Delta\rho/\rho)^{1/2}f^{-1} = 35.8 \times 10^3 \text{ m} \\
\gamma &= \beta/2\omega = 4.70 \times 10^{-5} \text{ m}^{-1} \text{ (latitude } \\
&\phi_0 = 35°, \omega = 1.99 \times 10^{-7} \text{ s}^{-1} \\
&\text{for a 1 year period)} \\
K_1 &= (\gamma^2 - R^{-2})^{1/2} = 3.78 \times 10^{-5} \text{ m}^{-1} \\
v_0 &= 0.2 \text{ m s}^{-1} \\
L &= (50-150) \text{ km} \\
Q &= 0.4 \times 10^5 \text{ m}^2 \text{ s}^{-1}.
\end{aligned}\right\} \quad (6.1)$$

Precise information of the $e$-folding scale $L$ is lacking and thus a range of $L$ values has been used. Our middle estimate of $L = 100$ km given in Section 2 is based on the fact that at a mooring 150 km north of CZ4 only a weak annual current signal was observed. To estimate $Q$, which appears only as a multiplicative factor in the model (a) solution, we set

$$Q = 2v_0L = 2 \times 0.2 \text{ m s}^{-1} \times 10^5 \text{ m}$$

$$= 0.4 \times 10^5 \text{ m}^2 \text{ s}^{-1}$$

since the total strength of the point source velocity model is $Q$ and

$$\int_{-\infty}^{\infty} v_0 \exp(-|y - y_0|/L)dy = 2v_0L \text{ for model (b)}.$$

Figure 10 shows, for the three subareas identified in Fig. 3, the theoretical wavenumber vector $\mathbf{k}$ associated with a wave located at the center of each region. To determine $\mathbf{k}$ for each case the polar coordinates of the subarea center were first found from Fig. 3. The centers of subareas 3, 4 and 5 have coordinates $(r, \theta) = (5000$ km, $197°)$, $(3400$ km, $206°)$, and $(2000$ km, $230°)$ respectively. From these $\theta$ values, $\delta (=\theta - \pi)$ and hence the ray along $\mathbf{c}_g$ for each

subarea were determined. The tip of the vector **k** was then located at the intersection of this ray and the slowness circle. The angle $\alpha$ for each subarea was measured from Fig. 10. The theoretical and observed values of $|\mathbf{k}|$ and $\alpha$ are given in Table 1, along with the computed values of wavelength and plane speed. For each subarea the theoretical direction of propagation agrees very well with the observed value. However, only for subarea 4 is the theoretical wavelength (299 km) in excellent agreement with the observed value (295 km). The discrepancy in subarea 3 (theoretical $\lambda$ too long) may be due to refraction, which is discussed in Section 7. The shortness of the theoretical $\lambda$ in subarea 5, which is just west of California, suggests generation of annual waves by a source off California (e.g., the coastal winds—see White and Saur, 1981) may also be important. The combined effect of the two sources would be a smaller group velocity angle $\delta$ (see Fig. 10) and hence a smaller value of $|\mathbf{k}|$ (i.e., a larger $\lambda$), which would agree better with the observed value of $\lambda$.

The observed amplitude distributions of the wave field variables are illustrated in Figs. 11 and 12. The vertical displacement at 300 m (Fig. 11) corresponds to $|d|$ as found in our theory, and the surface current speed (Fig. 12) corresponds to $|\mathbf{u}| = (|u|^2 + |v|^2)^{1/2}$. A notable feature common to both of these contour plots in the region west of 160°W is the pronounced monotonic increase of wave amplitude as one moves westward along any fixed latitude. To see whether either model (a) or model (b) solution could reproduce such a behavior, we completed $|d_{sa}|$, $|d_{sb}|$, $|\mathbf{u}|_{sa}$ and $|\mathbf{u}|_{sb}$ along the middle latitude 35°N ($y = 0$) at the three longitudes passing through the center of subareas 3, 4 and 5 (Table 2). Surprisingly, model (b) solution yields amplitude levels for $|d|$ and $|\mathbf{u}|$ that agree reasonably well with the observed values, with both quantities increasing to the west. (The reason for this unexpected behavior will be discussed later.) In contrast, the point source model (a) amplitudes tend to be much larger than the observed values and show little variation with longitude. Encouraged by the results for model (b) velocity profile, the zonal variation of $|d_{sb}|$ and $|\mathbf{u}|_{sb}$ for several points along 35°N was then found for different values of $L$ (Figs. 13 and 14). Figure 13 shows that for all $L$ in the range $50 \leqslant L \leqslant 150$ km, $|d_{sb}|$ increases monotonically to the west, although the curves tend to flatten out west of 170°W for small values of $L$ ($L = 50, 75$ km). For larger values of $L$ (100–150 km), the theory compares favorably with the data. Figure 14 shows that $|\mathbf{u}|_{sb}$ monotonically increases to the west for all $L$ values considered only up to 170°W. West of 170°W the monotonicity decreases as $L$ decreases until $L \leqslant 75$ km, in which case the current speed actually decreases to the west. Moreover the theory compares favourably with the data only between 140–170°W; west of 170°W the theoretical values are about half those observed.
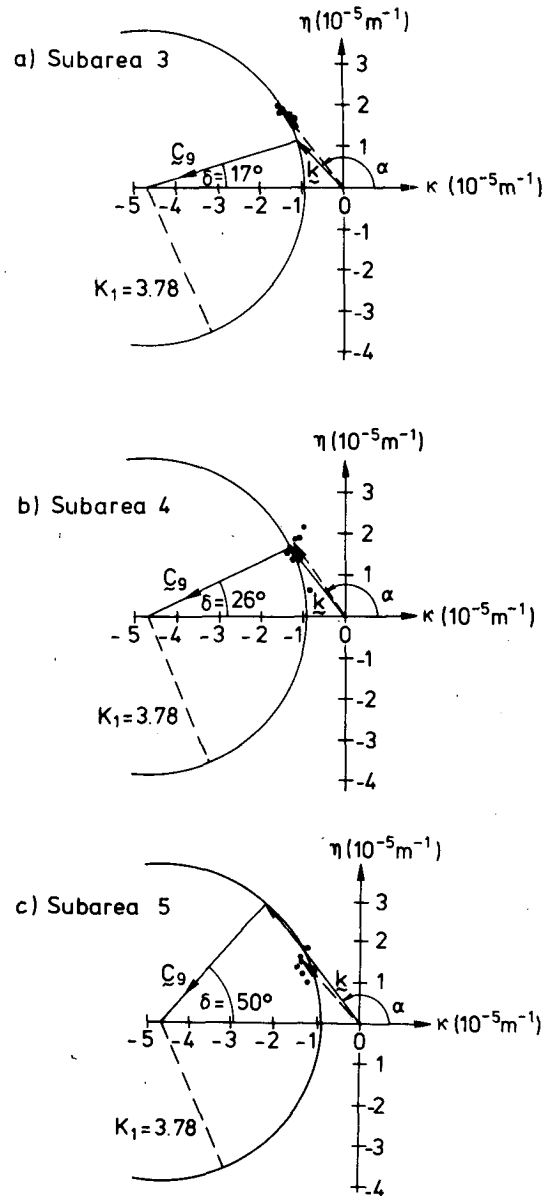


FIG. 10. Comparison between observed and theoretical wavenumber vectors for subareas 3, 4 and 5 (see Fig. 3). The data for subareas 3 and 4 were taken from KM's Fig. 7 and 6 respectively; the subarea 5 data were taken from KM's Table 1. The angle $\delta$ between $\mathbf{c}_g$ and the horizontal axis for each subarea is defined by the equation $\theta = \pi + \delta$, where $\theta$ is the polar angle of the ray from the source S in Fig. 8 (i.e., CZ4) to the center of that subarea.

To understand the surprising growing behavior of our solutions along $y = 0$ (35°N), contour plots of $|d|$ and $|\mathbf{u}|$ for $r > 500$ km were then computed. Figure 15 shows the model (b) vertical displacement at 300 m. Due west of the source (along $y = y_0$ or latitude 48°N), the solution falls off like $r^{-1/2}$ as expected since for $y = y_0$, $\theta = \pi$ and thus $|d_{sb}|$ is independent of $\theta$ [see (5.16)]. However, south of this latitude the con-

TABLE 1. Comparison between observed and theoretical wavenumber vectors for subareas 3, 4 and 5 (see Fig. 3). For subarea 3 the observed value of $|\mathbf{k}|$ is the average of eight values of $(\kappa^2 + \eta^2)^{1/2}$, where the $(\kappa, \eta)$ pairs come from the eight locations (38°N, 175°E), (38°N, 175°W), ..., (32°N, 175°E), (32°N, 175°W) given in Table 1 of KM. The observed value of $\alpha$ was estimated from Fig. 10a. The observed errors for $|\mathbf{k}|$ and $\alpha$ in subarea 3 were estimated from the Fig. 1 data in the eight vector space subareas contained in subarea 3. Similar remarks apply to the data for subareas 4 and 5; except in subarea 4, the lone data point with $|\kappa|$, $\eta < 1 \times 10^{-5}$ m$^{-1}$ (see Fig. 10b) was excluded. The prescription for finding the theoretical values of $\alpha$ and $|\mathbf{k}|$ are given in the text.

| | Subarea | $\alpha$ (deg) | $\begin{matrix}|\mathbf{k}|\\(10^{-5}\text{ m}^{-1})\end{matrix}$ | Wavelength, $\lambda = 2\pi/|\mathbf{k}|$ (km) | Phase speed $(c)$ (cm s$^{-1}$) |
|---|---|---|---|---|---|
| 3 | Observation | 130 ± 5 | 2.30 ± 0.30 | 273 (242–314) | 0.87 (0.77–1.00) |
| | Theory | 135 | 1.60 | 393 | 1.25 |
| 4 | Observation | 126 ± 7 | 2.13 ± 0.35 | 295 (253–353) | 0.94 (0.80–1.12) |
| | Theory | 129 | 2.10 | 299 | 0.95 |
| 5 | Observation | 133 ± 10 | 1.98 ± 0.30 | 317 (275–324) | 1.00 (0.87–1.19) |
| | Theory | 128 | 3.55 | 177 | 0.56 |

tours, for all three $L$ values, tend to slant upward toward the source and their values increase monotonically to the west. Thus, westward along a fixed southerly latitude, the $\theta$-dependence increases more rapidly than the decreasing $r^{-1/2}$ behavior, the net result being a monotonically increasing $|d_{sb}|$. Unfortunately, the general slant (or slope) of the theoretical contours in the observation region tends to be less than that observed by KM (Fig. 16).[4] This may be partly due to the fact that near CZ4 the coastline is oriented along a NNW–SSE axis, whereas in the theory a N–S alignment for the coastline is used. If the beam emanating out of CZ4 was downward toward the WSW, steeper contours would occur in the latitude band 30–40°N. In any event, the distributed coastal velocity model (b) appears to be more representative of nature than the point source velocity model (a). In the latitude band 30–40°N this latter model produces a fairly uniform $|d|$ west of 150°W (Fig. 17), in contrast to the observed pattern.
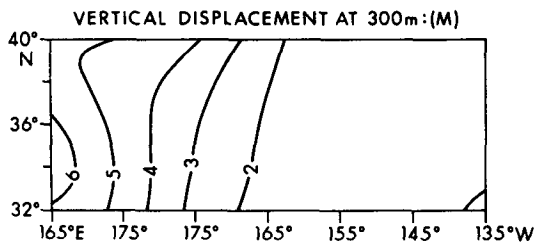
It is interesting to note here that some evidence of

VERTICAL DISPLACEMENT AT 300m:(M)



FIG. 11. Amplitudes of the vertical displacement associated with the analyzed annual baroclinic Rossby waves at 300 m depth (Kang and Magaard, 1980).

---

[4] Just before this paper went to press, Dr. Magaard informed me that in his latest analysis, the observed contours in the band 36–39°N were found to be more slanted toward CZ4 than those in KM (see Fig. 3 in Magaard, 1983). Thus the agreement between theory and observation is actually better than that shown in our Fig. 16.

an $r^{-1/2}$ behavior for a Rossby wave field west of Vancouver Island has been reported by Roden (1977). He observed 400–600 km wave disturbances in the North Pacific dynamic heights from the latitude band 20–50°N. Moreover, in the northerly band 43–47°N the amplitude of these waves at 158°W (see his Fig. 3) is larger than that at 177°W (his Fig. 2).

Figure 18 shows the current field for the model (b) coastal current, with $L$ as a parameter. For small $L$ the current field is dominated by a double-lobed pattern, whereas for large $L$ the field consists of a single narrow beam. For southerly latitudes the contours tend to slant upward toward the source (as in the case for $|d|$), again giving a westward increase of $|u|$ along a fixed latitude. However, the theoretical values tend to be less than those observed and the theoretical contours are almost orthogonal to those of KM (see Fig. 19). Moreover, in this case a downward tilting of the beam emanating from CZ4 does not improve matters significantly. However, comparison of Fig. 20 (point source coastal current) with the observations shown in Fig. 19 suggests that incorporating some aspects of a point source coastal current into a theory with a distributed coastal current could be fruitful. Indeed, our contour results forcefully indicate how important it is to have a detailed knowledge of the source. In effect we have here an "inverse problem" to solve: "Given the observed
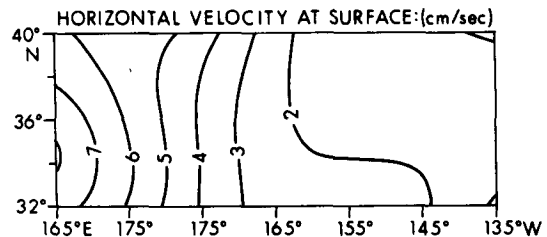
HORIZONTAL VELOCITY AT SURFACE:(cm/sec)



FIG. 12. Amplitudes of the horizontal particle velocity associated with the analyzed baroclinic Rossby waves at the sea surface (Kang and Magaard, 1980).

TABLE 2. Comparison between observed and theoretical vertical displacements and horizontal current speeds at three points along latitude 35°N ($y = 0$). The observed values were estimated by interpolation of the data in Figs. 11 and 12. The center of subareas 3, 4 and 5 (marked by crosses in Fig. 3) have polar coordinates $(r, \theta)$ = (5000 km, 197°), (3400 km, 206°) and (2000 km, 230°) respectively, where $r, \theta$ are measured from CZ4 (= point S in Fig. 8). Letters $a$) and $b$) refer to model (a) and (b) coastal current profiles in which $Q$ = $0.4 \times 10^5$ m² s⁻¹ for model (a) and $v_0 = 0.2$ m s⁻¹, $L = 100$ km for model (b).

| Center of subarea | | Vertical displacement $\|d\|$ at 300 m, (m) | $\|u\|$ (cm s⁻¹) | $\|v\|$ (cm s⁻¹) | Current speed $(\|u\|^2 + \|v\|^2)^{1/2}$ (cm s⁻¹) |
|---|---|---|---|---|---|
| 3 | Observation | 3.8 | — | — | 5 |
| | Theory $a$) | 10.8 | 4.3 | 4.2 | 6.0 |
| | Theory $b$) | 4.9 | 1.9 | 1.9 | 2.7 |
| 4 | Observation | ~1.75 | — | — | 1.9 |
| | Theory $a$) | 10.2 | 6.1 | 4.8 | 7.8 |
| | Theory $b$) | 2.7 | 1.6 | 1.3 | 2.1 |
| 5 | Observation | ~1.25 | — | — | ~1.6 |
| | Theory $a$) | 5.5 | 5.7 | 4.5 | 7.3 |
| | Theory $b$) | 0.6 | 0.6 | 0.5 | 0.8 |

far-field data shown in Figs. 11 and 12, what is the nature of the source?"

## 7. Discussion

In the above theory we have neglected the presence of a mean flow. Sufficiently strong lateral or vertical shears in a mean flow could lead to barotropic or baroclinic instabilities. Weak shears could result in wave refraction and critical layer absorption (Schoff et al., 1981). The incorporation of mean flow effects into the forced problem considered here is certainly of interest, but beyond the scope of the present paper.

Instead we shall briefly discuss the refraction of the waves due to a variable Coriolis parameter $f(y)$, with particular emphasis on trying to explain the wavelength discrepancy ($\lambda_{theor}$ too long) found for subarea 3 (see Fig. 10a). As mentioned in Section 6, the wavelength discrepancy ($\lambda_{theor}$ too short) found for subarea 5 (see Fig. 10c) is probably due to interference between the longer annual waves generated off the California coast, which have a westward group velocity,

and the shorter waves generated near CZ4. The resultant group velocity vector for the two wave fields in subarea 5 would be inclined to the horizontal at an angle of about $\delta = 25°$. A ray with this angle would pass through the middle of the data cluster in Fig. 10c and would yield a theoretical k very close to that observed.

From the dispersion relation (3.10), rewritten in the form

$$\omega = \frac{-\beta\kappa}{\kappa^2 + \eta^2 + f^2/g'H_0},$$  (7.1)

we find

$$c_g = \left(\frac{\partial\omega}{\partial\kappa}, \frac{\partial\omega}{\partial\eta}\right)$$

$$= \frac{\beta}{(k^2 + f^2/g'H_0)^2}[\kappa^2 - (\eta^2 + f^2/g'H_0), 2\kappa\eta],$$  (7.2)
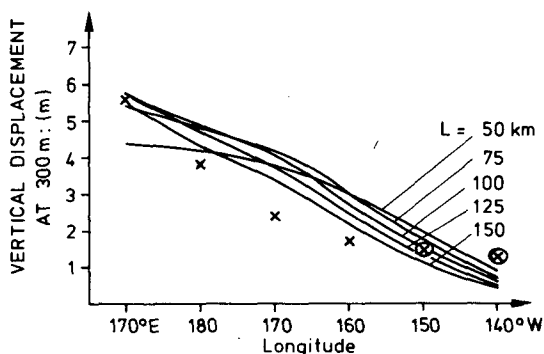


FIG. 13. Comparison between observed ($x$) and theoretical vertical displacements at 300 m depth along the latitude 35°N ($y = 0$). The theoretical curves, for different values of $L$, were computed from the model (b) asymptotic solution (5.16). The data was taken from Fig. 11. The circled crosses are rough estimates only, obtained by extrapolation of the data in Fig. 11.
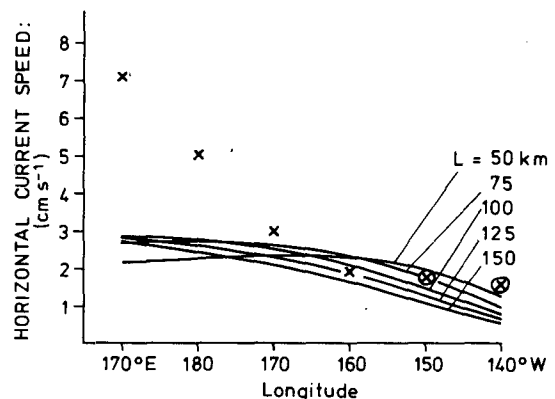


FIG. 14. Comparison between observed ($x$) and theoretical horizontal current speeds along the latitude 35°N ($y = 0$). The theoretical curves for different values of $L$, were computed from model (b) asymptotic solution $\|u\|_{sb} = (\|u_{sb}\|^2 + \|v_{sb}^2\|)^{1/2}$, where $u_{sb}$ and $v_{sb}$ are given by (5.19) and (5.22) respectively. The data were taken from Fig. 13. The circled crosses are rough estimates only, obtained by extrapolation of the data in Fig. 12.
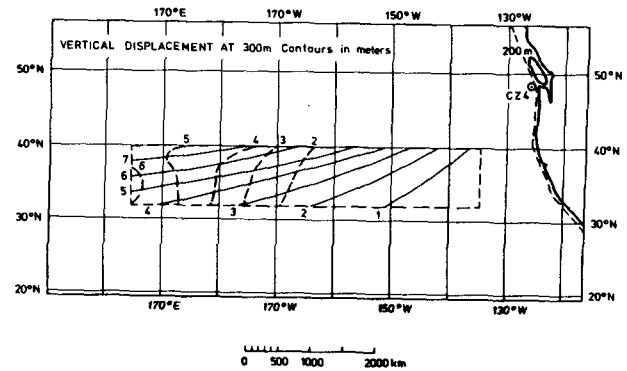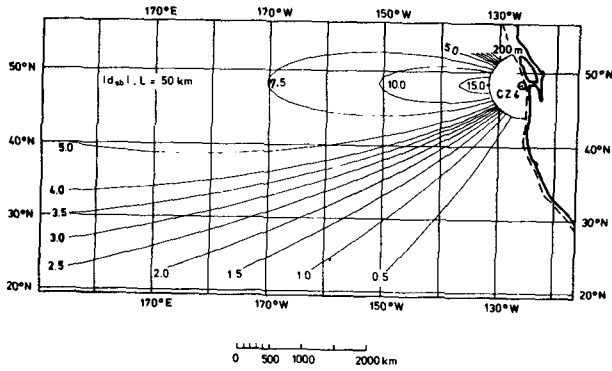
FIG. 15. Contours (in meters) of model (b) asymptotic solution $|d_{sb}|$ for $r > 500$ km, with different values of $L$.



FIG. 16. Comparison of the observed (dashed) and theoretical (solid) contours of vertical displacements at 300 m depth using model (b) with $L = 100$ km.
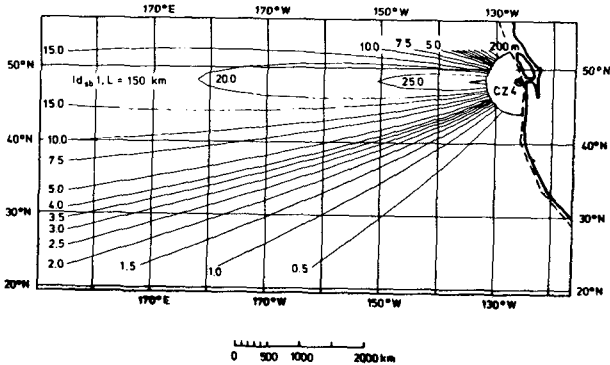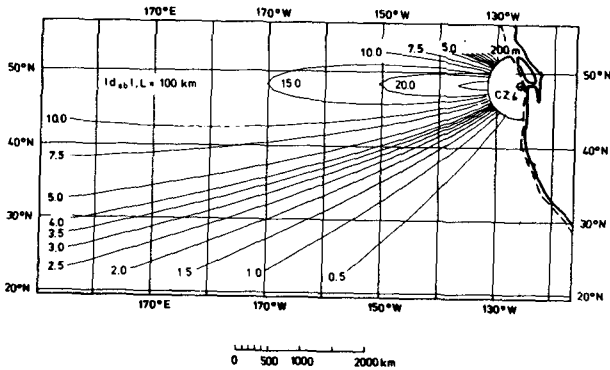
If we put $f = f_0 + \beta y$ in the dispersion relation (7.1), then the radius of the slowness circle, $K_1(y)$, decreases as $f$ increases (i.e., the latitude $y$ increases). Therefore near the high-latitude station CZ4, the coastally generated waves will have a $\mathbf{k}$ nearly pointed westward since the slowness circle has a relatively small radius compared to $\gamma$. Now, since the local topography is aligned NNW–SSE and Rossby waves are transverse, the oscillating boundary current near CZ4 will likely produce waves with $\mathbf{k}$ pointing in the WSW direction, as shown in Fig. 21. But such waves will have a $\mathbf{c}_g$ pointing toward the north and therefore will soon encounter the critical latitude for the annual wave. At the critical latitude the wave rays will be reflected, as shown in Fig. 21. Now the wave rays will be refracted towards the equator as the Rossby wave energy travels toward subarea 3, a region of smaller $f$. At the center of this subarea, $\mathbf{c}_g$ would be inclined to the horizontal at an angle of about $\delta = 30°$. For such a $\delta$, $\mathbf{c}_g$ would lie along a ray passing through the data cluster in Fig. 10a, yielding a $\mathbf{k}$ which agrees very favorably with the average wavenumber vector for subarea 3.

where $k^2 = \kappa^2 + \eta^2$. For $f$ a slowly varying function of $y$, it follows that along wave rays (group velocity trajectories) $\omega$ and $\kappa$ are invariant whereas $\eta = \eta(y)$ (e.g., see Schoff *et al.*, 1981). Thus according to (7.1), $\eta^2$ increases as $f^2$ decreases (and vice-versa), in a manner such that $\eta^2 + f^2/g'H_0$ remains constant. Hence (7.2) implies that the ratio $|\partial\omega/\partial\eta|/\partial\omega/\partial\kappa|$ increases as $f$ decreases. Therefore a WSW directed group velocity vector at high latitudes say, will be refracted toward the equator (as in Fig. 21). With this information in hand we now propose the following scenario for the energy propagation from CZ4 to the center of subarea 3.
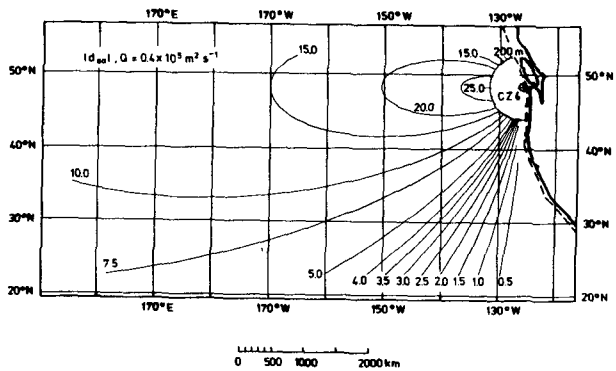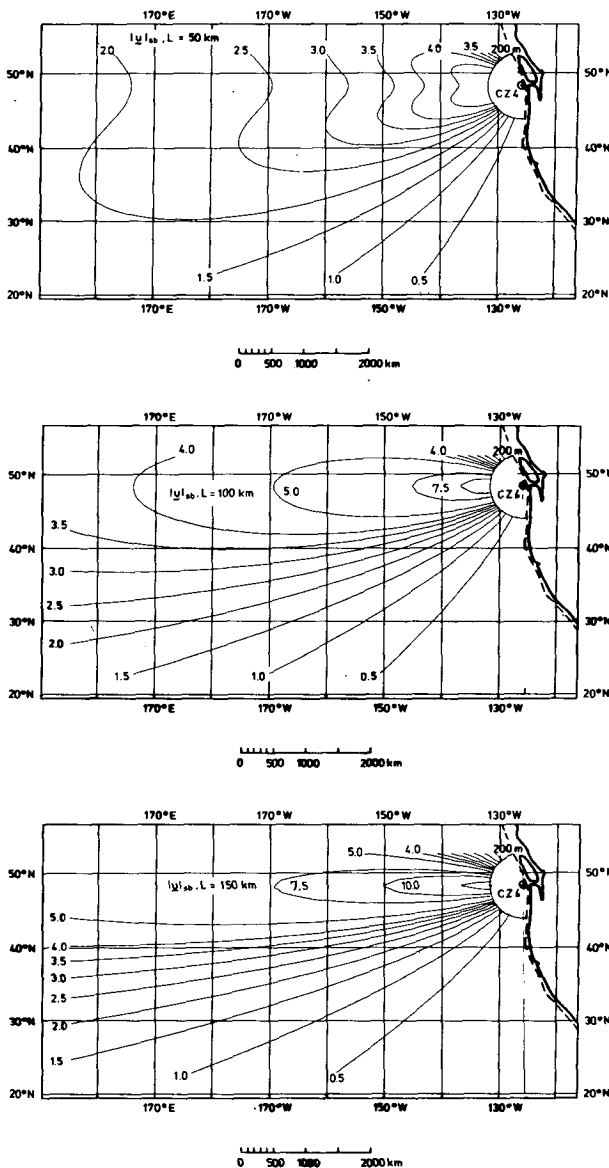


FIG. 17. Contours (in meters) of model (a) asymptotic solution $|d_{sa}|$ for $r > 500$ km obtained from (5.11) with $Q = 0.4 \times 10^5$ m$^2$ s$^{-1}$ ($=2v_0 L$ with $v_0 = 0.2$ m s$^{-1}$ and $L = 100$ km).

## 8. Summary and future work

We have shown that a fluctuating eastern boundary current of limited N–S extent can efficiently generate (annual-period) first baroclinic mode Rossby waves. West of the generating region centered at $(x, y)$ $= (0, y_0)$, the far-field wave amplitude falls off like $r^{-1/2}$, where $r$ is the radial distance from $(0, y_0)$. However, along a fixed latitude south of the source (i.e., along a fixed $y < y_0$), the wave amplitude increases to the west provided the N–S profile of the boundary current has a decaying character as $|y - y_0| \to \infty$. The far-field wave energy travels radially outward from the source. The phase, however, travels south-
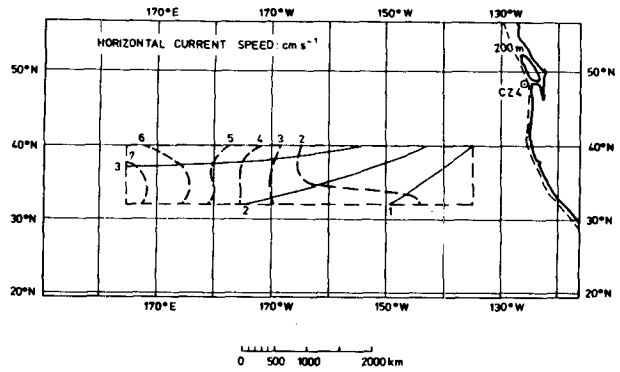


FIG. 19. Comparison of observed (dashed) and theoretical (solid) contours of horizontal current speed using model (b) with $L = 100$ km.

westward in the region $y > y_0$, westward along $y = y_0$ and northwestward in the region $y < y_0$.

The theory reasonably well explains many of the properties of the annual Rossby waves observed by KM. In the latitude band 30–40°N the theory accurately predicts the observed direction of phase propagation, and, to a lesser extent, the observed wavelength. Also, the westward increase observed in both the vertical displacement at 300 m ($|d|$) and the surface current speed ($|u|$) is qualitatively predicted by the theory for model (b) boundary current profile. However, the finer details of KM's two-dimensional maps of $|d|$ and $|u|$ are not accurately reproduced, especially in the case of $|u|$. Also, west of 170°W, the theoretical values of $|u|$ are only about half of those observed.

Although the theory was developed primarily to explain the observations of KM, its formulation, within the frame work of a reduced gravity model, is quite general. For example, the generation of first baroclinic mode waves of periods other than the annual could be investigated. Also, other forms of the
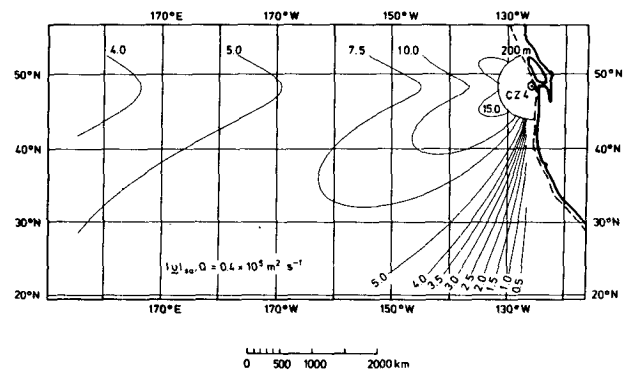






FIG. 18. Contours (in centimeters/second) of model (b) asymptotic solution $|u|$ for $r > 500$ km, with different values of $L$.



FIG. 20. Contours (in centimeters/second) of model (a) asymptotic solution $|u|_{sa} = (|u_{sa}|^2 + |v_{sa}|^2)^{1/2}$ for $r > 500$ km, where $u_{sa}$ and $v_{sa}$ are given by (5.13) and (5.15), respectively. $Q$ is the same as in Fig. 17.
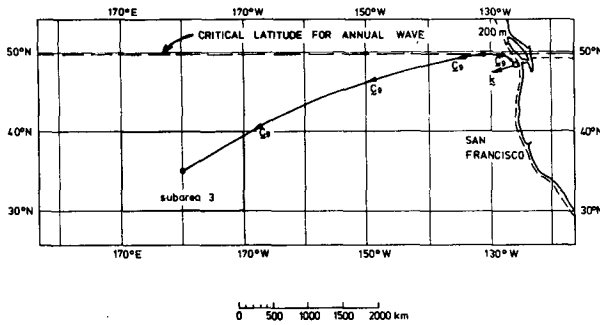
FIG. 21. Rossby wave refraction due to a
variable Coriolis parameter $f(y)$.

boundary current profile $v_c$ could be treated (e.g., a pair of point sources would be an interesting case). The only restriction on $v_c$ is that its Fourier transform must exist.

We regard the theory presented in this paper as a first approximation to what may be needed to fully explain all the details of KM's observations. In this spirit, we suggest here several ways in which the theory could be extended and hopefully improved:

1) Determination of the ray paths emanating from CZ4 using the WKB method (or method of multiple scales) for a slowly varying $f$.

2) Investigation of the effect of source orientation and structure on the far field behavior. Also, determination of the response due to both a fluctuating coastal current and a variable coastally-confined windstress (e.g., as used in White and Saur, 1981).

3) Determination of mean flow effects, such as refraction and critical layer absorption.

4) Extension of model to include aegeostrophic phenomena such as Kelvin waves and mid-ocean surface and subsurface fronts.

In closing we also recommend that the proposed theory be tested with further field measurements of both temperature and current. Also, determination of the wind field would be of interest. One significant outcome of the theory is that a detailed knowledge of the structure of the coastal velocity profile is important. Thus, several moorings near CZ4 are necessary. Beyond this region, the moorings could be arranged[5] to test the following theoretical predictions:

1) The $r^{-1/2}$ behavior of the far field ($r \geq 200$ km) along latitude 48°N (through CZ4).

2) The existence of the critical latitude near 50°N for the annual wave.

3) The structure of the far-field radiation pattern

---

[5] Since the annual waves travel so slowly (~0.5–1 km/day for $c_g$), some of the measurements could be done in a "leapfrog" manner. For example, sensors placed at CZ4 for a two year period to study the generation process could then be moved to a location 700 km west or southwest of CZ4 to detect the incoming wave energy which would take several years to travel this distance.

as per Figs. 15 and 18 on two or three circles centered at CZ4 and with radii of 250, 500 and 1000 km.

4) The existence of an annual oscillation of the axis of the surface west-wind drift west of the British Columbia–Washington coast.

REFERENCES

Abramowitz, M., and I. A. Stegun, Eds., 1965: *Handbook of Mathematical Functions.* Dover, 1046 pp.

Campbell, G. A., and R. M. Foster, 1948: *Fourier Integrals for Applications.* Van Nostrand, 177 pp.

Gallegos-Garcia, A., W. J. Emery, R. O. Reid and L. Magaard, 1981: Frequency-wavenumber spectra of sea surface temperature and wind-stress curl in the eastern North Pacific. *J. Phys. Oceanogr.,* **11,** 1059–1077.

Huyer, A., E. J. C. Sobey and R. L. Smith, 1979: The spring transition in currents over the Oregon continental shelf. *J. Geophys. Res.,* **84,** 6995–7011.

Kang, Y. Q., 1980: Low frequency temperature fluctuations in the upper 400 meters of the central North Pacific. Ph.D. dissertation, University of Hawaii, 131 pp.

——, and L. Magaard, 1979: Stable and unstable Rossby waves in the North Pacific Current as inferred from mean stratification. *Dyn. Atmos. Oceans,* **3,** 1–14.

——, and ——, 1980: Annual baroclinic Rossby waves in the central North Pacific. *J. Phys. Oceanogr.,* **10,** 1159–1167.

Kirwan, A. D., G. J. McNally, E. Reyna and W. J. Merrell, 1978: The near-surface circulation in the eastern North Pacific. *J. Phys. Oceanogr.,* **8,** 937–945.

Krauss, W., and C. Wuebber, 1982: Response of the North Atlantic to annual wind variations along the eastern coast. *Deep-Sea Res.,* **29,** 851–864.

LeBlond, P. H., and L. A. Mysak, 1978: *Waves in the Ocean.* Elsevier, 602 pp.

Magaard, L., 1977: On the generation of baroclinic Rossby waves in the ocean by meteorological forces. *J. Phys. Oceanogr.,* **7,** 359–364.

——, 1983: On the potential energy of baroclinic Rossby waves in the North Pacific. *J. Phys. Oceanogr.,* **13,** 38–42.

Mysak, L. A., and P. H. LeBlond, 1972: The scattering of Rossby waves by a semi-infinite barrier. *J. Phys. Oceanogr.,* **2,** 108–114.

——, and A. J. Willmott, 1981: Forced trench waves. *J. Phys. Oceanogr.,* **11,** 1481–1502.

Roden, G. I., 1977: On long-wave disturbance of dynamic height in the North Pacific. *J. Phys. Oceanogr.,* **7,** 41–49.

Schoff, P. S., D. L. T. Anderson and R. Smith, 1981: Beta-dispersion of low-frequency Rossby waves. *Dyn. Atmos. Oceans,* **5,** 187–214.

White, W. B., and J. F. T. Saur, 1981: A source of annual baroclinic waves in the eastern subtropical North Pacific. *J. Phys. Oceanogr.,* **11,** 1452–1462.